Title

Designed metalloprotein stabilizes a semiquinone radical.

Permalink

https://escholarship.org/uc/item/9v8290jw

Journal

Nature Chemistry, 8(4)

Authors

Ulas, Gözde
Lemmin, Thomas
Gassner, George
et al.

Publication Date

2016-04-01

DOI

10.1038/nchem.2453

Peer reviewed

Designed metalloprotein stabilizes a semiquinone radical

Gözde Ulas[1], **Thomas Lemmin**[1], **Yibing Wu**[1], **George T. Gassner**[2], and **William F. DeGrado**[1,*]

[1]Department of Pharmaceutical Chemistry, University of California – San Francisco, San Francisco, California 94158, USA

[2]Department of Chemistry and Biochemistry, San Francisco State University, San Francisco, California 94132, USA

Abstract

Enzymes use binding energy to stabilize their substrates in high-energy states that are otherwise inaccessible at ambient temperature. Here we show that a *de novo* designed Zn(II) metalloprotein stabilizes a chemically reactive organic radical that is otherwise unstable in aqueous media. The protein binds tightly to and stabilizes the radical semiquinone form of 3,5-di-*tert*-butylcatechol. Solution NMR spectroscopy in conjunction with molecular dynamics simulations show that the substrate binds in the active site pocket where it is stabilized by metal–ligand interactions as well as by burial of its hydrophobic groups. Spectrochemical redox titrations show that the protein stabilized the semiquinone by reducing the electrochemical midpoint potential for its formation via the one-electron oxidation of the catechol by approximately 400 mV (9 kcal mol^{-1}). Therefore, the inherent chemical properties of the radical were changed drastically by harnessing its binding energy to the metalloprotein. This model sets the basis for designed enzymes with radical cofactors to tackle challenging chemistry.

How to dial functions in a protein is the key question in protein engineering. *De novo* protein design has proved to be a powerful tool to pinpoint the structural features that determine function within proteins—a minimized protein scaffold is systematically varied and tested to engineer new functions[1–11]. One of the key questions in protein design is to understand how a protein's environment can direct the properties of the bound cofactor or substrate. In previous studies, optimization of the electrostatic and hydrophobic interactions guided the tuning of cofactors like haem and flavins in affinity, reduction potentials and O2 binding[12–14]. A series of designed three-helix coiled coils with mononuclear Zn(II) to mimic carbonic anhydrase were shown to activate water for ester hydrolysis and CO_2 hydration[15–17]. An artificial metallo-β-lactamase was designed to self-assemble into a

tetramer and use catalytic Zn(II) sites to hydrolyse β-lactams. The enzyme was functional in *E. coli*, where it hydrolysed the β-lactam antibiotic, ampicillin, which resulted in cell survival[18]. Our group studied designed Due Ferri (DF) proteins[19] as models for natural non-haem di-iron proteins, and showed that subtle modifications to the first- and second-coordinating spheres of the site were able to direct the O_2-dependent chemistry[20]. Recently, protein design was used to trap the unstable coplanar conformation of a *p*-biphenylalanine residue[21]. Here we extend the use of rational protein design to stabilize a chemically unstable species—an organic radical.

Enzymes efficiently use radicals, an unstable and generally highly reactive species, in challenging chemical transformations. These radicals are not destructive like the reactive oxygen species because they are 'controlled'; that is, (1) generated during catalytic turnover and quenched at the end, and (2) contained in the enzymatic environment to prevent any undesired off-pathway reactivity. However, the mechanism by which enzymes stabilize these otherwise kinetically and thermodynamically unstable species remains poorly understood. Protein engineering has been used to test principles of radical stabilization through the *de novo* design of 'maquette' proteins with covalently attached radical-forming amino acids Trp$^{\bullet}$ and Tyr$^{\bullet}$ or mercaptophenol derivatives[22–25]. Although it has been possible to stabilize Tyr$^{\bullet}$ kinetically with half-lives up to six seconds[26], they were thermodynamically destabilized by approximately 100 mV relative to the corresponding small molecule in aqueous solution[24,27]. Here we focus on the thermodynamic and kinetic stabilization of *ortho*-semiquinones, which are radical intermediates in essential redox processes and catalysis in nature[28–31]. The 3,5-di-*tert*-butyl-semiquinone radical anion (SQ$^{\bullet}$), a small-molecule analogue of native *o*-semiquinone radicals, is the one-electron oxidized intermediate in the redox triad 3,5-di-*tert*-butylcatechol/semiquinone/*o*-benzoquinone (QH_2/SQ$^{\bullet}$/Q) (Fig. 1a). Although SQ$^{\bullet}$ is naturally less stable than QH_2 and Q, its thermodynamic potential can be shifted. In aprotic organic solvents, coordination to cations[32,33] and transition-metal ions[34–36] stabilizes the SQ$^{\bullet}$. In organic solvents the presence of Zn(II) ($[Zn(H_2O)_6]^{2+}$) shifts the one-electron reduction potential of Q, $E_{Q/SQ^{\bullet}}$, by ~220 mV compared with the free SQ$^{\bullet}$ in solution, which makes the Zn(II)–SQ$^{\bullet}$ complex more stable by 5 kcal mol^{-1} (ref. 34). In aqueous buffers only a two-electron reduction of Q to QH_2 is observed, and SQ$^{\bullet}$ is undetectable under steady-state conditions[37].

We previously used QH_2 as a substrate for a di-Fe(III) bound DF protein variant, DF3[38]. In the catalytic cycle, QH_2 is first oxidized to Q by di-Fe(III). The dimetal centre is then re-oxidized by ambient O_2 to di-Fe(III) to complete the catalytic turnover. As the di-Fe(III) centre catalyses two-electron chemistry, the substrate was converted from QH_2 into Q, and no SQ$^{\bullet}$ intermediate was observed. We rationalized that a redox-inert transition metal should be used to observe and stabilize SQ$^{\bullet}$ instead. Here we used the single-stranded form of DF-type proteins, DFsc, in which we exchanged the Fe(III) with Zn(II). The DFsc variant used in this work, 2A3H-DFsc (referred to as DFsc) binds two Zn(II) to form [DFsc-Zn(II)$_2$], a well-structured four-helix bundle (PDB 2LFD)[20].

We hypothesized that inherent chemical properties of SQ$^{\bullet}$ could be used to distinguish it from QH_2 and Q, and guide its binding to [DFsc-Zn(II)$_2$]; the SQ$^{\bullet}$ radical is the predominant form of the compound at neutral pH (pK_a = 6)[39], and is an excellent chelator of Zn(II)

(Supplementary Table 1). In contrast, Q is a poor chelator, and is observed to dissociate away from Zn(II) when Zn(II)–Q is electrochemically generated from Zn(II)–SQ• (ref. 35). QH_2 mono- and dianions are minor species in solution at neutral pH ($pK_a = 10$)[39], which means that binding to Zn(II) is also unlikely to result from the thermodynamic cost of deprotonation. Moreover, SQ• is stabilized in apolar solvents relative to water, and therefore binding to the hydrophobic cleft of DFsc should stabilize the SQ• by removing the radical from bulk water.

In this study, we show that [DFsc-Zn(II)₂] strongly stabilizes SQ• over the otherwise more stable QH_2 and Q forms. Optical and magnetic spectroscopy, along with spectrochemical redox titrations, demonstrate that the binding of SQ• to DFsc effectively pulls the equilibrium towards SQ• given a mixture of 1:1 Q:QH_2. By examining derivatives of QH_2 we show that tight binding and radical stabilization requires the presence of the hydrophobic *t*-butyl groups, which are partially buried on interaction with the protein. Molecular dynamics (MD) simulations were used to gain further insight into the structural characteristics of the [DFsc-Zn(II)₂]–SQ• complex. Taken together, these results established how binding energy can be harnessed to stabilize an otherwise inaccessible radical.

Results and discussion

Optical and magnetic spectroscopy methods were used to confirm SQ• binding to DFsc and define the new characteristics of the radical in the protein environment. When [DFsc-Zn(II)₂] was added to an equimolar mixture of Q and QH_2, the equilibrium shifted to favour the corresponding SQ• (Fig. 1b), as evidenced by a large decrease in the absorption band of Q ($\lambda_{max} = 415$ nm) and the appearance of a new broad band that spanned 740–850 nm (Fig. 2a), typical of a Zn(II)-bound SQ• radical[35]. An isosbestic point at 492 nm suggests the lack of additional intermediates. A strong band at the position of the SQ• was also observed in the circular dichroism spectrum (Supplementary Fig. 2), which suggests that the achiral SQ• is bound to DFsc in a unique asymmetric conformation. Taken together, optical spectroscopy indicates that the *in situ* generated SQ• is in complex with the metal-bound DFsc, and yields the [DFsc-Zn(II)₂]–SQ• moiety. The SQ• is most probably bound to the Zn(II), as the absorption features closely match that of small molecule Zn(II)–SQ• complexes (Supplementary Table 1).

Factors that direct SQ• binding were evaluated by using derivatives of QH_2 or Q, which were examined for SQ• formation. *o*-Quinones/catechols with electron-releasing or electron-withdrawing substituents, such as –OMe, –NO₂ and –H, do not form SQ• in the presence of [DFsc-Zn(II)₂] (Supplementary Fig. 3). Therefore, it is unlikely that the *t*-butyl groups play an electronic role in binding. The only variant to form SQ• was 4-*t*-butylcatechol, with a lower yield than its di-*t*-butyl analogue, which highlights the importance of the hydrophobic *t*-butyl groups in the tight binding and, thus, stability of SQ• in the context of the protein.

Room-temperature electron paramagnetic resonance (EPR) spectra confirmed the formation of the paramagnetic SQ• radical in complex with [DFsc-Zn(II)₂]. The spectrum of [DFsc-Zn(II)₂]–SQ• is consistent with the presence of an organic radical ($g = 2.003$). The signal is broadened (peak-to-peak line-width, 8 Gauss) and lacks hyperfine features, which suggests

the immobilization of the SQ• radical. Overlaid spectra of SQ• generated in the presence of [DFsc-Zn(II)$_2$], apo DFsc or Zn(II) are shown in Fig. 2b. Spin quantification shows a yield of $72 \pm 7\%$ radical formation in the presence of [DFsc-Zn(II)$_2$] (with respect to the protein). The apo DFsc control does not show any trace of a radical. The Zn(II)-only control showed a low yield of radical formation (2% yield).Although it is expected that Zn(II) would partially stabilize SQ• (refs 34,40), the radical experiences a markedly different environment in the protein, as evidenced by the line-shape differences of [DFsc-Zn(II)$_2$]–SQ•, Zn(II)-only and SQ•-only spectra (Fig. 2b and Supplementary Fig. 6).

The midpoint reduction potential of [DFsc-Zn(II)$_2$]–SQ• was determined by a series of redox titrations with dithionite in the presence of a redox indicator dye (potassium indigo tetrasulfonate (ITS)) under anaerobic conditions at neutral pH (Supplementary Fig. 4). Relative populations of [DFsc-Zn(II)$_2$]–SQ• (λ_{max} = 740 nm) and oxidized ITS (λ_{max} = 594 nm, $E_{mid,7}$ = −46 mV)[41] under steady-state conditions were determined, and fit in the Nernst equation to yield the midpoint potential $E_{mid,7}$ = −21 mV versus NHE for the reduction of [DFsc-Zn(II)$_2$]–SQ• at neutral pH, a value that is ~400 mV less than the reported reduction potential of free SQ• in aqueous solution[39]. This finding indicates that [DFsc-Zn(II)$_2$]–SQ• is strongly stabilized in the protein environment (by 9 kcal mol^{-1}).

Solution NMR spectroscopy confirmed the structure and paramagnetic nature of the [DFsc-Zn(II)$_2$]–SQ• complex. The bound organic radical caused considerable paramagnetic relaxation enhancement (PRE) of the backbone amides, observed as a significant decrease in the corresponding peak intensity[42]. To determine which backbone resonances are affected by the SQ• radical anion, ^{15}N heteronuclear single quantum coherence (HSQC) spectra (Fig. 2c) were recorded before and after the addition of the substrate to reach a 74% conversion to [DFsc-Zn(II)$_2$]–SQ•. As PRE that resulted from a radical with an isotropic g factor is not expected to yield pseudocontact shifts or residual dipolar coupling, reassignment of the residues in [DFsc-Zn(II)$_2$]–SQ• was not necessary[42,43]. Residues that experienced a significant decrease in peak intensity were then mapped onto the solution NMR structure of [DFsc-Zn(II)$_2$] (Fig. 3). The highest peak-intensity decrease that was detected was found in residues proximal to the active site, consistent with the SQ• binding at the active site.

To interpret our results further, we used MD to gain insights into the structural properties of the [DFsc-Zn(II)$_2$]–SQ• complex. First, a metadynamics simulation was used to sample possible conformations of the SQ• when interacting with the di-Zn(II) site. The two collective variables used defined the distance and angle between the centre of mass of the SQ• oxygen atoms and the Zn(II) ions. An ensemble of 20 different interacting conformers (3.0 Å distance cutoff) were then used to seed individual 50 ns MD simulations, summing up to a total of 1 μs. The SQ• binding was characterized by an enlargement of the helix 1 and 2 interface, which allowed the SQ• to interact directly with the Zn(II) cations (Fig. 4 and Supplementary Fig. 5). A total of 10,000 snapshots were then clustered to yield three different conformations (root mean square deviation of the centroids was less than 1.5 Å over the Zn(II)–SQ• site). Each centroid structure was further optimized using a Gaussian09 ONIOM QM/MM[44] (quantum mechanics/molecular mechanics) method and all converged to a single geometry, in which the semiquinone was bound to the only coordinatively unsaturated Zn(II) as a bidentate ligand.

The resulting structure is consistent with a SQ•-bound conformation. A notable feature is the sequestration of the *t*-butyl groups in a very hydrophobic pocket adjacent to the di-Zn(ɪɪ) site surrounded by the apolar side chains of A10, G14, I17, A43, G47, V50 and Y51 (Fig. 4c). Favourable interactions with the protein cleft would contribute to the binding of SQ•, an observation also validated by the lack of SQ• formation in derivatives missing the *t*-butyl groups. A major difference of the SQ•-bound DFsc model is the change in the coordination number of the active site Zn(ɪɪ). The di-Zn(ɪɪ) are five- and six-coordinate in the starting structure, [DFsc-Zn(ɪɪ)$_2$] (ref. 20), and both become six-coordinate in the SQ•-bound state. The only His ligand (H107) to the pentavalent Zn(ɪɪ) in [DFsc-Zn(ɪɪ)$_2$] dissociates to create a tetravalent Zn(ɪɪ), which then acquires SQ• to become six-coordinate. This finding is consistent with the expectation that SQ• binding would require a coordinatively unsaturated metal site, and provides an indication that a His rotation could be responsible in forming the tetravalent Zn(ɪɪ) intermediate. It is interesting that in the structure of an alternative oxidase with a related di-iron active site, proximal His ligands show variable coordination to iron depending on substrate and inhibitor binding (3VVA, PDB http://www.pdb.org/pdb/search/structidSearch.do?structureId=3VVA)[45].

Based on the computational model, we hypothesized that mutating H107 could leave the Zn(ɪɪ) four-coordinate in the [DFsc-Zn(ɪɪ)$_2$] state and so be more available for the bidentate SQ• binding. Variants of DFsc in which H107 was mutated to the non-coordinating residues Ala and Asn were made and characterized. Spectral titrations indicated that H107A-DFsc and H107N-DFsc variants bind approximately 2.3 equiv. Zn(ɪɪ) per protein (versus the theoretical value of 2 equiv. (Supplementary Fig. 10)). Interestingly, both variants form SQ• complexes more rapidly than the wild-type DFsc (Supplementary Fig. 8), which confirms the hypothesis that Zn(ɪɪ) loses a ligand to become four coordinate on SQ• binding. The variants also form a 4-*t*-butylcatechol-derived SQ• complex, reminiscent of the wild-type DFsc (Supplementary Fig. 9). These findings are consistent with our prediction that H107 is not necessary for protein–SQ• complex formation.

In conclusion, we used a designed metalloprotein to stabilize successfully the SQ• radical anion using binding energy to pull the equilibrium towards the otherwise unstable SQ• state at room temperature in aqueous medium. Through optical and magnetic spectroscopic characterization, we demonstrate that SQ• is bound to the metalloprotein, most probably anchored to Zn(ɪɪ) as a bidentate ligand, and is encased within the protein when bulk solvent is removed. Structural analogues of SQ• provide further insight that one of the crucial driving forces is favourable hydrophobic interactions with the cleft of the protein. Computational modelling of the bound structure allowed us to rationalize our results further, which are consistent with the requirement for hydrophobic interactions initiated by the *t*-butyl groups and Zn(ɪɪ)-binding in enhancing the binding energy to drive the equilibrium towards the otherwise unstable SQ•. We assessed that the protein–SQ• complex is stabilized by 10^6–10^7 (9 kcal mol^{-1}) in comparison with the free radical SQ• in neutral solution. Thus, these studies lead to a deeper understanding of how proteins stabilize radical species.

Methods

Ultraviolet/visible (UV/vis) spectroscopy

DFsc was dissolved in 50 mM MOPS (pH 7.0) and 100 mM NaCl to 50–100 μM concentration. The protein was reconstituted with $Zn(\text{II})$ by adding $ZnSO_4$ stock in milliQ water to the protein in a 2:1 $Zn(\text{II})$:protein ratio and incubated at room temperature for one hour. After incubation, the $[DFsc\text{-}Zn(\text{II})_2]$ solution was transferred to a quartz cuvette (1 cm pathlength, Starna Cells) and the initial spectra recorded with a Cary 300 Bio UV/vis spectrophotometer. Substrates, premixed in a separate vessel (Q:QH_2 in a 1:1 ratio, dissolved in dimethylformamide (DMF)), were added to the protein solution, and then quickly mixed by pipetting. Derivatives were screened under identical conditions, with 4-*t*-butylcatechol, 4-nitrocatechol, 3-methoxycatechol and catechol added to the protein solution in ten molar equivalents, and incubated overnight to air oxidize.

EPR spectroscopy

Measurements were performed with a Bruker EMX EPR spectrometer (Bruker Instruments). All the measurements were performed at room temperature (298 K). The spectra were recorded at a frequency of 9.83 GHz, with a microwave power of 25 mW, modulation amplitude of 3 Gauss and modulation frequency of 100 kHz. Each spectrum was collected as an average of three scans, sweeping 100 Gauss. The protein sample contained 50 μM [DFsc-$Zn(\text{II})_2$] in 50 mM MOPS (pH 8.0), 100 mM NaCl. To the protein solution, Q was added to yield 1 mM (stock solution in DMF), followed by the addition of NADH (stock solution in milliQ) to yield 500 μM. A 25 μl aliquot of this mixture was transferred to a 25 μl micropipette (Drummond, Wiretrol) and sealed with clay at one end.

NMR spectroscopy

The DFsc was labelled with ^{15}N by bacterial expression in M9 minimal medium supplemented with [15]NH_4Cl (Sigma-Aldrich). Two-dimensional (2D) ^{15}N-HSQC spectra were collected at 25 °C on a Bruker Avance-I 800 MHz spectrometer with a 5 mm *x,y,z*-shielded pulse-field gradient triple resonance probe. The protein (640 μM) was reconstituted with 2.5 molar equivalents of $ZnSO_4$ in 100 mM MOPS (pH 7.51), 100 mM NaCl; 5% (v/v) D_2O was added before data collection. To the protein solution, 213 μM of *N*-acetyl-^{15}N,[13]C-glycine (synthesized following the literature protocol[46]) was added as the internal concentration standard. After the [DFsc-$Zn(\text{II})_2$] spectrum was recorded, 5 equiv. of the Q (400 mM stock prepared in 1:1 DMF:MeOH mixture) and 2.5 equiv. of NADH (500 mM stock prepared in milliQ) were added to the sample. UV/vis spectroscopy of the sample indicated that this resulted in a 74% conversion to the [DFsc-$Zn(\text{II})_2$]–$SQ^{\bullet}$ complex. 2D ^{15}N-HSQC spectra were recorded along t_1(^{15}N) and t_2(^{1}H) with, respectively, 128 and 2,048 complex points, and $t_{1,max}$(^{15}N) = 30 ms and $t_{2,max}$(^{1}H) = 91 ms. The ^{1}H chemical shift was referenced to the water line at 4.74 ppm and ^{15}N chemical shifts were referenced indirectly via gyromagnetic ratios. The ^{15}N carrier frequency was set at 119 ppm. NMR data were processed, analysed and visualized using NMRPipe[47] and Sparky[48]. Prior to Fourier transformation, time-domain data were performed by linear prediction once, multiplied by the esine square bell window functions shifted by 75° and zero-filled once.

Equilibrium spectrochemical redox titrations

DFsc (100 μM) was reconstituted with 200 μM Zn(II) in 50 mM MOPS (pH 7.0) and 100 mM NaCl, and the SQ$^\bullet$ complex was formed by adding a premixed mixture of 1:1 Q:QH$_2$ to yield 200 μM each in the final concentration. After overnight incubation with the Q:QH$_2$ mixture (at ambient temperature and atmosphere), the solution was spun down and sterile filtered. To this solution, a redox indicator dye (dye, ITS, with midpoint reduction potential at neutral pH, $E_{m,7}$ = −46 mV versus NHE)[41] was added in a 2 μM concentration. The sample was then transferred to an anaerobic quartz chamber and degassed by sequential vacuum pumping and purging with N$_2$(g). The quartz chamber was fitted with a 250 μl Hamilton Gastight syringe containing degassed 1.6 mM sodium dithionite solution. After an initial spectrum collection, a 5 μl aliquot of the dithionite solution was introduced into the 700 μl protein solution (equivalent to 10 μM dithionite per injection), mixed and left to equilibrate for 60 minutes, at which point a spectrum of the final equilibrated state was collected. Dithionite was added in increments of 5 μl until the SQ$^\bullet$ signal no longer decreased. Absorbances at 596 and 740 nm were used to follow the oxidized dye and SQ$^\bullet$ concentrations, respectively. Concentrations of the oxidized dye and SQ$^\bullet$ were set to 100% in the absence of dithionite (black spectrum in Supplementary Fig. 4). Populations of oxidized dye and SQ$^\bullet$ were thus quantified as a ratio for each spectrum collected after equilibrium was reached following each dithionite aliquot addition. Under equilibrium conditions, a common solution potential is reached[49], and we can assume that the E_{ref} equals E_{SQ}, as shown in equation (1). The ratio of oxidized-to-reduced dye measured from each spectrum and the known E_{ref} for the dye were used to calculate the E_m for the semiquinone in the SQ$^\bullet$/QH$_2$ couple (where QH$_2$ is 3,5-di-t-butylcatechol (DTBC)).

$$E_{\mathrm{m}}^{\mathrm{ref}} - \frac{RT}{nF}\ln\frac{[\mathrm{Dye_{red}}]}{[\mathrm{Dye_{ox}}]} = E_{\mathrm{m}}^{\mathrm{SQ}} - \frac{RT}{nF}\ln\frac{[\mathrm{DTBC}]}{[\mathrm{SQ}]} \quad (1)$$

Supplementary Material

Refer to Web version on PubMed Central for supplementary material.

Acknowledgments

References

1. DeGrado WF, Summa CM, Pavone V, Nastri F, Lombardi A. *De novo* design and structural characterization of proteins and metalloproteins. Annu. Rev. Biochem. 1999; 68:779–819. [PubMed: 10872466]

2. Dürrenberger M, Ward TR. Recent achievements in the design and engineering of artificial metalloenzymes. Curr. Opin. Chem. Biol. 2014; 19:99–106. [PubMed: 24608081]

3. Faiella M, Roy A, Sommer D, Ghirlanda G. *De novo* design of functional proteins: toward artificial hydrogenases. Biopolymers. 2013; 100:558–571. [PubMed: 24281721]

4. Hill RB, Raleigh DP, Lombardi A, DeGrado WF. *De novo* design of helical bundles as models for understanding protein folding and function. Acc. Chem. Res. 2000; 33:745–754. [PubMed: 11087311]

5. Kaplan J, DeGrado WF. *De novo* design of catalytic proteins. Proc. Natl Acad. Sci. USA. 2004; 101:11566–11570. [PubMed: 15292507]

6. Kiss G, Celebi-Olcum N, Moretti R, Baker D, Houk KN. Computational enzyme design. Angew. Chem. Int. Ed. 2013; 52:5700–5725.

7. Watkins DW, Armstrong CT, Anderson JLR. *De novo* protein components for oxidoreductase assembly and biological integration. Curr. Opin. Chem. Biol. 2014; 19:90–98. [PubMed: 24607598]

8. Zastrow ML, Pecoraro VL. Designing functional metalloproteins: from structural to catalytic metal sites. Coord. Chem. Rev. 2013; 257:2565–2588. [PubMed: 23997273]

9. Koga N, et al. Principles for designing ideal protein structures. Nature. 2012; 491:222–227. [PubMed: 23135467]

10. Lu Y, Yeung N, Sieracki N, Marshall NM. Design of functional metalloproteins. Nature. 2009; 460:855–862. [PubMed: 19675646]

11. Petrik ID, Liu J, Lu Y. Metalloenzyme design and engineering through strategic modifications of native protein scaffolds. Curr. Opin. Chem. Biol. 2014; 19:67–75. [PubMed: 24513641]

12. Farid TA, et al. Elementary tetrahelical protein design for diverse oxidoreductase functions. Nature Chem. Biol. 2013; 9:826–833. [PubMed: 24121554]

13. Lichtenstein BR, et al. Engineering oxidoreductases: maquette proteins designed from scratch. Biochem. Soc. Trans. 2012; 40:561–566. [PubMed: 22616867]

14. Bhagi-Damodaran A, Petrik ID, Marshall NM, Robinson H, Lu Y. Systematic tuning of heme redox potentials and its effects on O_2 reduction rates in a designed oxidase in myoglobin. J. Am. Chem. Soc. 2014; 136:11882–11885. [PubMed: 25076049]

15. Cangelosi VM, Deb A, Penner-Hahn JE, Pecoraro VL. A *de novo* designed metalloenzyme for the hydration of CO_2 . Angew. Chem. Int. Ed. 2014; 53:7900–7903.

16. Yu F, et al. Protein design: toward functional metalloenzymes. Chem. Rev. 2014; 114:3495–3578. [PubMed: 24661096]

17. Zastrow ML, Pecoraro VL. Designing hydrolytic zinc metalloenzymes. Biochemistry. 2014; 53:957–978. [PubMed: 24506795]

18. Song WJ, Tezcan FA. A designed supramolecular protein assembly with *in vivo* enzymatic activity. Science. 2014; 346:1525–1528. [PubMed: 25525249]

19. Calhoun JR, et al. Artificial diiron proteins: from structure to function. Biopolymers. 2005; 80:264–278. [PubMed: 15700297]

20. Reig AJ, et al. Alteration of the oxygen-dependent reactivity of *de novo* Due Ferri proteins. Nature Chem. 2012; 4:900–906. [PubMed: 23089864]

21. Pearson AD, et al. Trapping a transition state in a computationally designed protein bottle. Science. 2015; 347:863–867. [PubMed: 25700516]

22. Hay S, Westerlund K, Tommos C. Moving a phenol hyrdoxyl group from the surface to the interior of a protein: effects on the phenol potential and pK_A . Biochemistry. 2005; 44:11891–11902. [PubMed: 16128591]

23. Ravichandran KR, Liang L, Stubbe J, Tommos C. Formal reduction potential of 3,5-difluorotyrosine in a structured protein: insight into multistep radical transfer. Biochemistry. 2013; 52:8907–8915. [PubMed: 24228716]

24. Tommos C, Skalicky JJ, Pilloud DL, Wand AJ, Dutton PL. *De novo* proteins as models of radical enzymes. Biochemistry. 1999; 38:9495–9507. [PubMed: 10413527]

25. Tommos C, Valentine KG, Martínez-Rivera MC, Liang L, Moorman VR. Reversible phenol oxidation and reduction in the structurally well-defined 2-mercaptophenol-α$_3$C protein. Biochemistry. 2013; 52:1409–1418. [PubMed: 23373469]

26. Glover SD, et al. Photochemical tyrosine oxidation in the structurally well-defined α₃Y protein: proton-coupled electron transfer and a long-lived tyrosine radical. J. Am. Chem. Soc. 2014; 136:14039–14051. [PubMed: 25121576]

27. Berry BW, Martínez-Rivera MC, Tommos C. Reversible voltammograms and a Pourbaix diagram for a protein tyrosine radical. Proc. Natl Acad. Sci. USA. 2012; 109:9739–9743. [PubMed: 22675121]

28. Dooley DM, et al. A Cu(i)-semiquinone state in substrate-reduced amine oxidases. Nature. 1991; 349:262–264. [PubMed: 1846226]

29. Kalyanaraman B, Felix CC, Sealy RC. Semiquinone anion radicals of catechol(amine)s, catechol estrogens, and their metal ion complexes. Environ. Health Perspect. 1985; 64:185–198. [PubMed: 3007089]

30. Land EJ, Ramsden CA, Riley PA. Tyrosinase autoactivation and the chemistry of *ortho*-quinone amines. Acc. Chem. Res. 2003; 36:300–308. [PubMed: 12755639]

31. Mure M. Tyrosine-derived quinone cofactors. Acc. Chem. Res. 2004; 37:131–139. [PubMed: 14967060]

32. Peover ME, Davies JD. The influence of ion-association in the polarography of quinones in dimethylformamide. J. Electroanal. Chem. 1963; 6:46–53.

33. Chung TD, et al. Electrochemical behavior of calix[4]arenediquinones and their cation binding properties. J. Electroanal. Chem. 1995; 396:431–439.

34. Stallings MD, Morrison MM, Sawyer DT. Redox chemistry of metal–catechol complexes in aprotic media. 1. Electrochemistry of substituted catechols and their oxidation products. Inorg. Chem. 1981; 20:2655–2660.

35. Bodini ME, Copia G, Robinson R, Sawyer DT. Redox chemistry of metal–catechol complexes in aprotic media. 5. 3,5-Di-*tert*-butylcatecholato and 3,5-di-*tert*-butylsemiquinonato complexes of zinc(ii). Inorg. Chem. 1983; 22:126–129.

36. Benelli C, Dei A, Gatteschi D, Pardi L. Electronic and CD spectra of catecholate and semiquinonate adducts of zinc(ii) and nickel(ii) tetraaza macrocyclic complexes. Inorg. Chem. 1989; 28:1476–1480.

37. Guin PS, Das S, Mandal PC. Electrochemical reduction of quinones in different media: a review. Int. J. Electrochem. 2011; 2011:1–22.

38. Faiella M, et al. An artificial di-iron oxo-protein with phenol oxidase activity. Nature Chem. Biol. 2009; 5:882–884. [PubMed: 19915535]

39. Jovanovic SV, Kónya K, Scaiano JC. Redox reactions of 3,5-di-*tert*-butyl-1,2-benzoquinone. Implications for reversal of paper yellowing. Can. J. Chem. 1995; 73:1803–1810.

40. Kalyanaraman B, Premovic PI, Sealy RC. Semiquinone anion radicals from addition of amino acids, peptides, and proteins to quinones derived from oxidation of catechols and catecholamines. J. Biol. Chem. 1987; 262:11080–11087. [PubMed: 3038907]

41. Tratnyek PG, et al. Visualizing redox chemistry: probing environmental oxidation–reduction reactions with indicator dyes. Chem. Educator. 2001; 6:172–179.

42. Clore GM, Iwahara J. Theory, practice, and applications of paramagnetic relaxation enhancement for the characterization of transient low-population states of biological macromolecules and their complexes. Chem. Rev. 2009; 109:4108–4139. [PubMed: 19522502]

43. Otting G. Protein NMR using paramagnetic ions. Annu. Rev. Biophys. 2010; 39:387–405. [PubMed: 20462377]

44. Dapprich S, Komáromi I, Byun KS, Morokuma K, Frisch MJ. A new ONIOM implementation in Gaussian 98. 1. The calculation of energies, gradients and vibrational frequencies and electric field derivatives. J. Mol. Struct. (Theochem). 1999; 462:1–21.

45. Shiba T, et al. Structure of the trypanosome cyanide-insensitive alternative oxidase. Proc. Natl Acad. Sci. USA. 2013; 110:4580–4585. [PubMed: 23487766]

46. Herbst RM, Shemin D. Acetylglycine. Org. Synth. Coll. 1943; 2:1.

47. Delaglio F, et al. NMRPipe: a multidimensional spectral processing system based on UNIX pipes. J. Biomol. NMR. 1995; 3:277–293. [PubMed: 8520220]

48. San Francisco: University of California; SPARKY 3.

49. Dutton PL. Redox potentiometry: determination of midpoint potentials of oxidation–reduction components of biological electron-transfer systems. Methods Enzymol. 1978; 54:411–435. [PubMed: 732578]

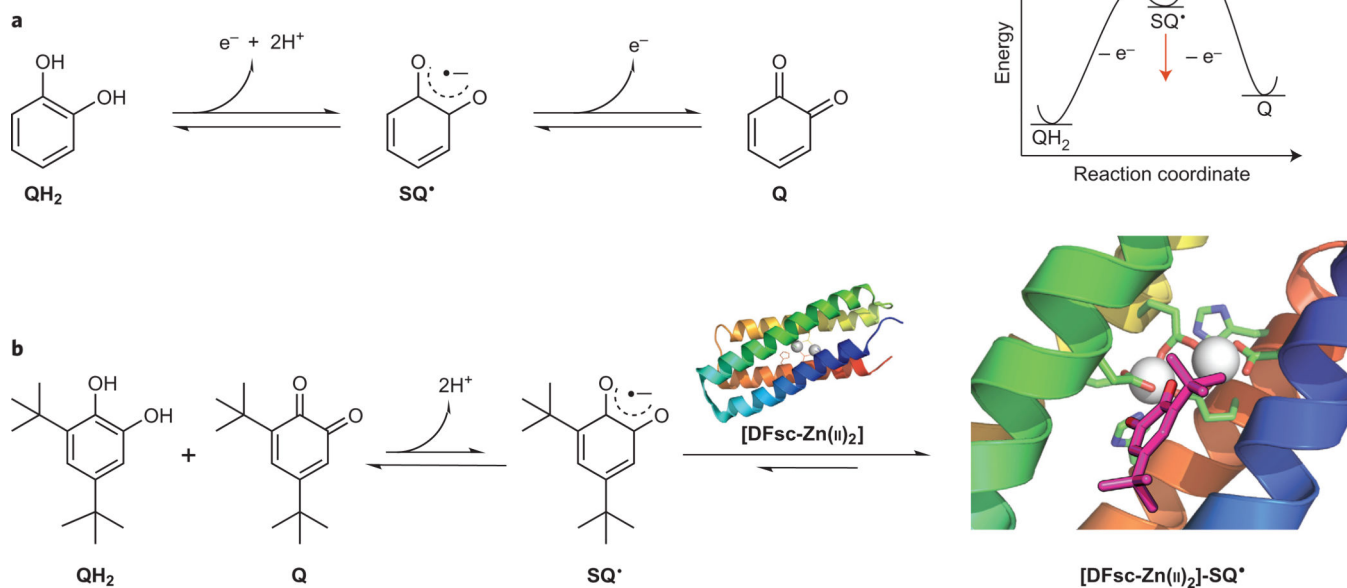50. The PyMOL Molecular Graphics System, Version 1.3r1. Schrödinger: LLC; 2010.

Figure 1. Semiquinone is unstable as a free radical, but its stability can be tailored in a protein environment

a, Scheme of a canonical equilibrium between QH_2, the anion radical $SQ^\bullet$ and Q. The $SQ^\bullet$ anion radical is an intermediate between the fully reduced QH_2 and the fully oxidized Q. The corresponding energy versus reaction coordinate plot is representative of the expected differences in thermodynamic potential for each discrete oxidation state. The red arrows indicate that the environment of $SQ^\bullet$ can change the $SQ^\bullet$ stability by shifting its thermodynamic potential. **b**, General scheme for reconstituting DFsc with a radical. $SQ^\bullet$ is generated *in situ* via comproportionation of QH_2 and Q and consumed by disproportionation as a free radical. In the presence of Zn(II)-bound DFsc ([DFsc-Zn(II)$_2$]), the equilibrium is shifted towards the otherwise unstable $SQ^\bullet$, which complexes with the protein to form [DFsc-Zn(II)$_2$]–$SQ^\bullet$.
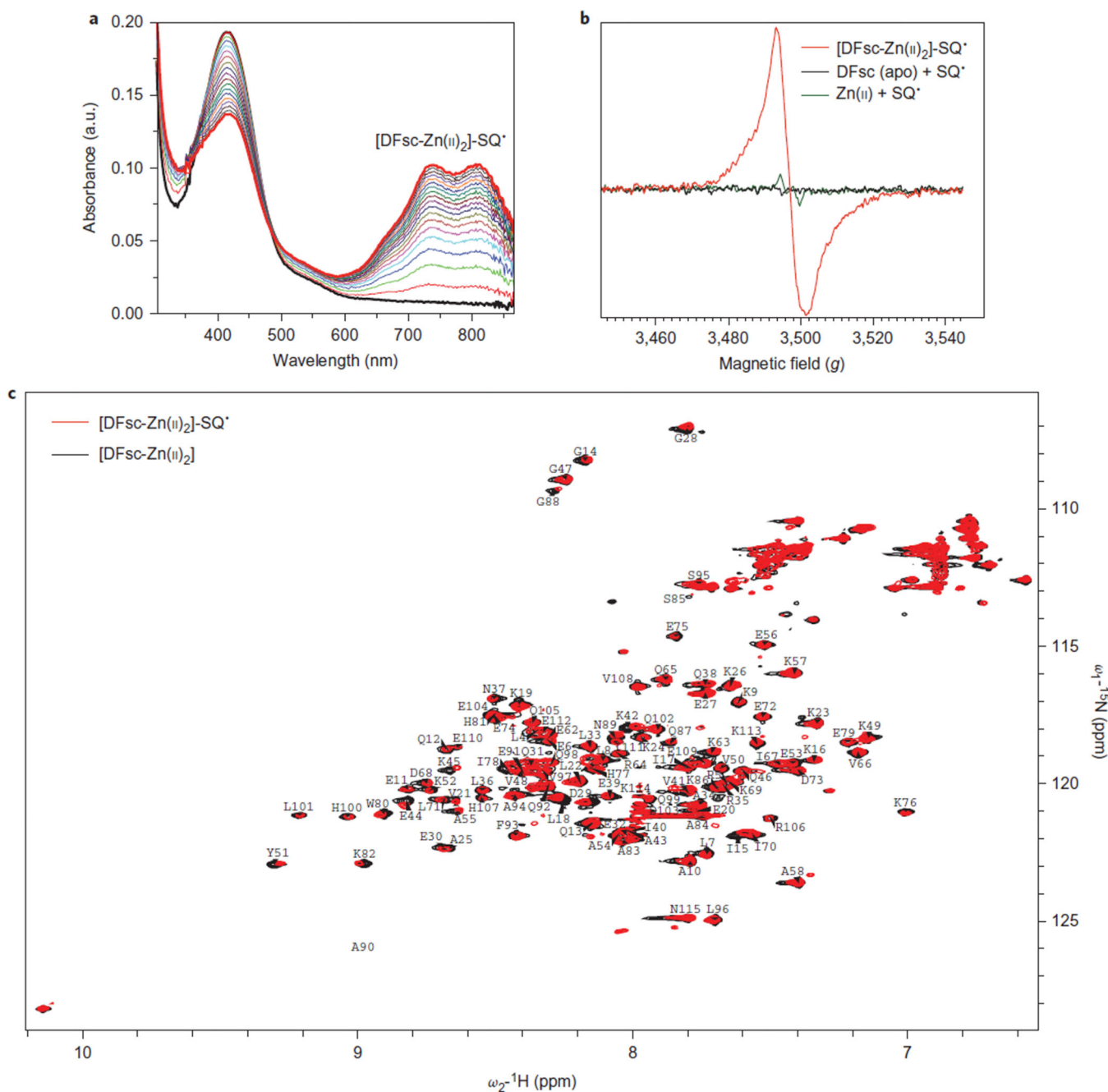
Figure 2. Observation of SQ• in complex with the *de novo* metalloprotein [DFsc-Zn(II)₂] by optical and magnetic spectroscopy

a, UV/vis absorption spectra were recorded starting from the time of QH₂ and Q mixing to generate SQ• *in situ* (black line), and at ten minute intervals up to 180 minutes (red line) (a.u., arbitrary units). **b**, EPR spectra of [DFsc-Zn(II)₂], apo DFsc and Zn(II) in the presence of SQ• generated *in situ*. **c**, 2D HSQC spectra of [DFsc-Zn(II)₂] (black) and after 74% of all the protein was converted into [DFsc-Zn(II)₂]–SQ• (red). Backbone assignments are labelled and are in good agreement with previous studies[20]. All amide resonances are visible at this contour level except for A90.
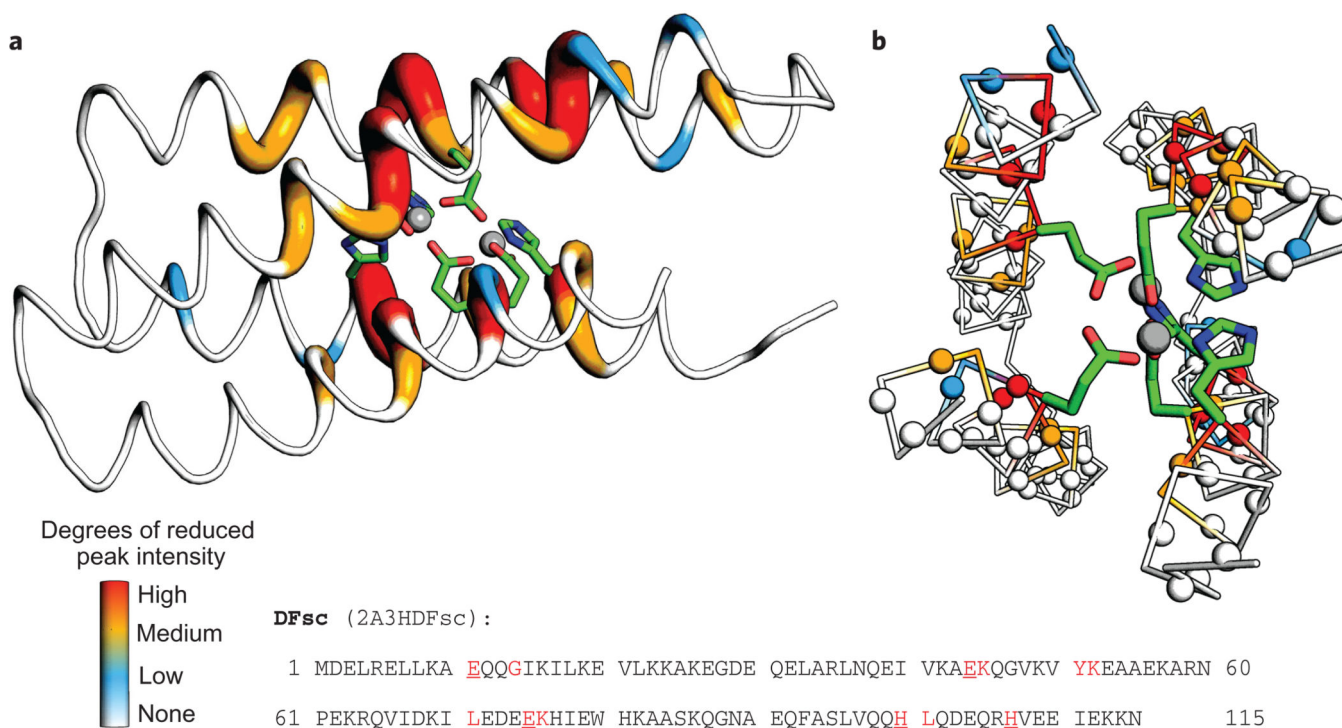
Figure 3. Analysis of results extracted from the [DFsc-Zn(II)$_2$]–SQ$^\bullet$ HSQC spectra colour-mapped on the [DFsc-Zn(II)$_2$] structure (PDB 2LFD), with the relative degrees of peak intensities compared

a,b, The highest degree of reduced peak intensity corresponds to the highest PRE. Colour-mapped structures are from the side (**a**), and top-down views, with the backbone amide nitrogen atoms displayed as spheres and the loop regions omitted for clarity (**b**). For both panels, Zn(II) is shown as grey spheres and Zn(II)-coordinating residues as sticks. Residues that experience the highest PRE are coloured red on the structural models and below in the corresponding sequence. Residues that coordinate to Zn(II) are underlined in the sequence. All molecular graphics were generated with PyMOL[50].
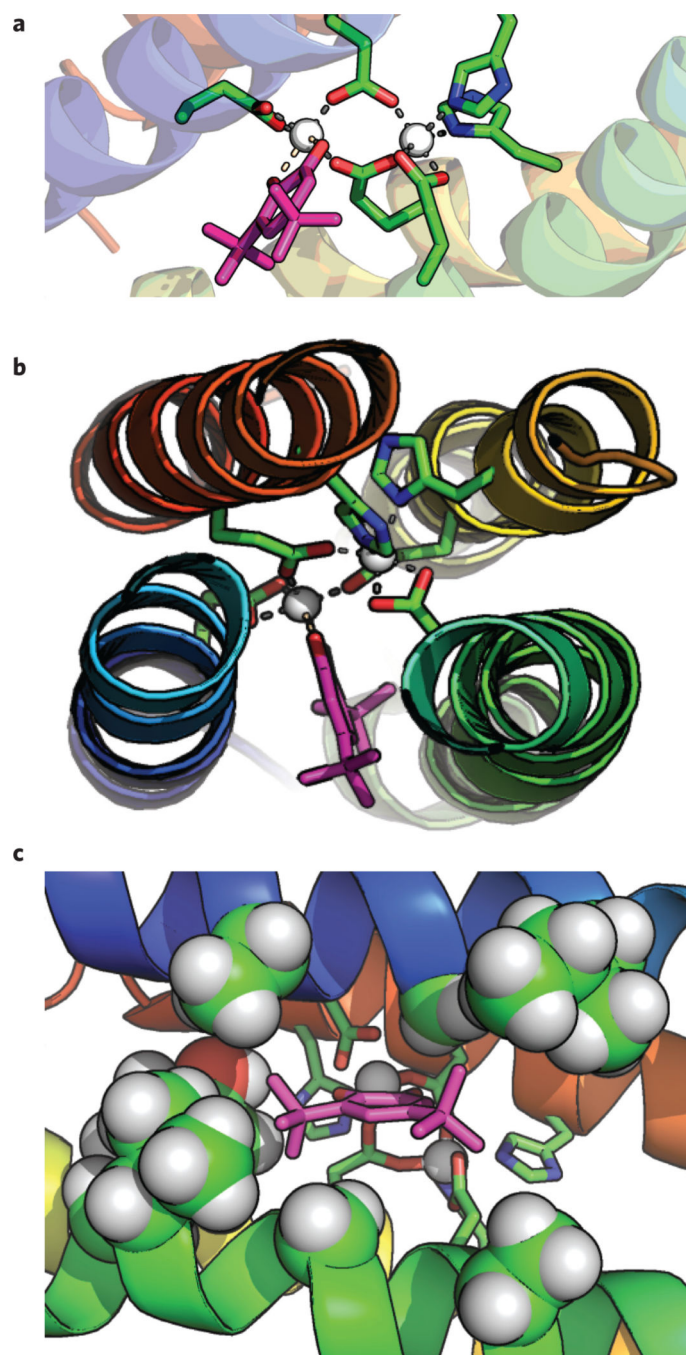
Figure 4. QM/MM-optimized model of [DFsc-Zn(ıı)₂]–SQ•

a, View of the DFsc active site showing the first coordination shell of the di-Zn(ıı) (white spheres), with the SQ• coloured magenta. Dashed lines indicate bonds. **b**, Top-down view of the [DFsc-Zn(ıı)₂]–SQ• complex showing the enlargement of helix 1 (blue) and helix 2 (green) to accommodate SQ• binding. **c**, View of the hydrophobic residues that line the helix 1 and 2 interface (shown as spheres: A10, G14, I17, A43, G47, V50, Y51), which interact with the *t*-butyl groups of SQ• (in magenta).